Key Points:
- The observed middepth (200-1,500 m) zonal currents in the equatorial Indian Ocean are characterized by a pronounced semiannual cycle exhibiting upward phase propagation
- The vertical propagation of middepth zonal currents is controlled by first-meridional-mode semiannual period Rossby wave that propagates energy downward
- The middepth Rossby waves are generated by wind-forced semiannual Kelvin waves that reflect at the eastern boundary

Vertical Propagation of Middepth Zonal Currents Associated With Surface Wind Forcing in the Equatorial Indian Ocean

Ke Huang[1], Michael J. McPhaden[2] (iD), Dongxiao Wang[1,3] (iD), Weiqiang Wang[1,4] (iD), Qiang Xie[1,4,5], Ju Chen[1], Yeqiang Shu[1], Qiang Wang[1] (iD), Jian Li[1], and Jinglong Yao[1]

[1]State Key Laboratory of Tropical Oceanography, South China Sea Institute of Oceanology, Chinese Academy of Sciences, Guangzhou, China, [2]Pacific Marine Environmental Laboratory, National Oceanic and Atmospheric Administration, Seattle, WA, USA, [3]School of Marine Sciences, Sun Yat-sen University, Guangzhou, China, [4]Laboratory for Regional Oceanography and Numerical Modeling, Qingdao National Laboratory for Marine Science and Technology, Qingdao, China, [5]Institute of Deep-Sea Science and Engineering, Chinese Academy of Sciences, Sanya, China

Abstract The vertical propagation of middepth (200–1,500 m) zonal velocity in the equatorial Indian Ocean (EIO) and its relationship with surface wind forcing are investigated. We focus on semiannual time scales, using in situ mooring observations and an oceanic reanalysis product that can reasonably well reproduce the structure and magnitude of the observed middepth zonal velocity in the EIO. The pronounced semiannual cycle in observed middepth zonal currents indicates a clear upward phase propagation with particularly robust signatures at depths of 500–1,000 m between 3°S to 3°N, 70 to 85°E. The main characteristics of the middepth currents are consistent with vertically propagating first-meridional-mode Rossby wave at semiannual period. Theory suggests that equatorial Kelvin waves, forced by zonal wind variations in the western half of the basin, transfer energy downward and eastward, reflecting into Rossby waves at the eastern boundary. These reflected Rossby waves transfer energy downward and westward, contributing greatly to observed phase propagation at middepths in the EIO.

1. Introduction

The zonal circulation in the equatorial Pacific, Atlantic, and Indian Oceans differs in several aspects, resulting from a variety of spatial and temporal scales and a complex pattern of mean zonal currents and countercurrents (e.g., Brandt et al., 2016; Cane & Moore, 1981; Chen et al., 2015; Duan et al., 2016; Han et al., 1999; Jensen, 1993; Nagura & McPhaden, 2016; Philander & Chao, 1991; Rao et al., 2017; D. Wang et al., 2004; F. Wang et al., 2016). These rich flow structures extend from the upper layers (0–200 m) to middepths (200–1,500 m), where earlier studies have documented the oceanic dynamic response to atmospheric forcing (Eriksen, 1981; Firing, 1987; Luyten & Swallow, 1976; Wyrtki, 1973; Youngs & Johnson, 2015).

In the equatorial Pacific and Atlantic Oceans, the middepth zonal currents beneath the pycnocline are equatorially trapped and transient, with strong annual variability (Brandt & Eden, 2005; Fischer & Schott, 1997; Gouriou et al., 2006; F. Wang et al., 2016). They are associated with surface wind forcing and have pronounced vertical phase propagation. Previous studies have suggested that forced equatorial waves can explain the vertically propagating equatorial zonal currents in the Pacific and Atlantic Oceans (Brandt & Eden, 2005; Marin et al., 2010). This is because the zonal velocity fluctuations at middepth appear to be dominated by equatorial nondispersive Rossby waves, which, having been generated by the reflection of the directly wind-driven Kelvin waves at the eastern boundary, propagate phase upward and westward compared with energy downward (Boning & Schott, 1993; Brandt & Eden, 2005; Kawase, 1987; Kessler & McCreary, 1993; Marin et al., 2010; Thierry et al., 2004).

In the equatorial Indian Ocean (EIO), several studies have found that middepth zonal currents are seasonal velocity reversal with strong semiannual variability (e.g., Jensen, 1993; Luyten & Roemmich, 1982). These currents appear to be ubiquitous features of the equatorial middepth circulation system, but a complete understanding of their dynamics has remained elusive. Luyten and Roemmich (1982) first presented a 1-year moored velocity record beneath the pycnocline in the western EIO and found that the variations in the zonal currents displayed pronounced upward phase propagation, potentially caused by linear equatorial long Rossby waves of the first-meridional-mode. Gent et al. (1983) used a linear ocean model to simulate the observations of Luyten and Roemmich (1982) and concluded that retention of reflecting lateral boundaries

and the superposition of baroclinic equatorial waves were important in producing the semiannual oscillation in the western EIO. Jensen (1993) applied a linear isopycnal ocean model to study semiannual variability in the EIO and demonstrated that well-simulated reversals of middepth zonal current and their distinct variations in the amplitude were the result of low baroclinic Kelvin and Rossby wave responses to wind forcing at semiannual periods. Jensen (1993) further postulated, consistent with the earlier work of Cane and Moore (1981), that an equatorial basin resonance could explain the observed strong semiannual variability in the EIO in which wind-driven and boundary-generated waves of the second baroclinic mode constructively interfered with one another to generate enhanced semiannual variability in zonal velocity (Han et al., 1999, 2011; Ogata & Xie, 2011; Yuan & Han, 2006). A subsequent study of this basin resonance in the EIO by Huang et al. (2018) highlighted the influence of second baroclinic mode on middepth semiannual variability and the distinct amplitude structure of the middepth zonal currents. Their analysis of moored observations also indicated an apparent vertical phase propagation in zonal velocity, which they hypothesized to be the result of the sum of second-order and other low-order baroclinic equatorial Kelvin and Rossby waves (e.g., Gent, 1981; McCreary, 1984). In other words, in addition to the effects of a second baroclinic mode resonance on the middepth variability in the EIO, the superposition of additional baroclinic modes introduces vertical propagation that is absent when just a single vertical mode is energized. The question to be addressed in this study is whether the variations in the middepth zonal current and associated vertical phase propagation can be understood in terms of the propagation of energy along raypaths governed by the equatorial wind-driven wave dynamics.

Analytically, the complete solution to the momentum equations can be separated into different meridional modes, for example, Kelvin and Rossby modes, with the vertical propagation of energy represented along equatorial rays associated with the group velocity of these different meridional modes (McCreary, 1984; Philander, 1978). The most pronounced rays in the solution are associated with Kelvin and low meridional mode Rossby waves, in which the Kelvin ray appears to be directly wind driven and the Rossby rays both wind driven and generated by reflection at the eastern boundary (McCreary, 1984). Dewitte and Reverdin (2000) for annual variability in the Pacific, and Thierry et al. (2004) and Brandt and Eden (2005) for semi-annual and annual variability in the Atlantic, found that variations at middepths in the ocean were related to the presence of Rossby rays generated by the reflection of wind-driven Kelvin ray at the eastern boundary. Recently, Huang et al. (2018) used model based sensitivity experiments that included boundary damping to find that the energy from reflected Rossby waves was in phase but stronger than that due to directly wind-forced Rossby waves. Herein, we will test the hypothesis that vertical energy propagation from boundary-generated Rossby waves is important in effecting the vertical structure of middepth zonal currents in the EIO.

Analyses of the longest near-surface records collected in the equatorial eastern Indian Ocean, combined with oceanic reanalysis and modeling experiments, have indicated that the surface and subsurface zonal currents are seasonally propagating in a complex manner in response to surface wind forcing (Chen et al., 2015; Duan et al., 2016; Iskandar et al., 2009; McPhaden, 1982; Nagura & McPhaden, 2016; Sengupta et al., 2007). In this study, we use middepth moored records and an oceanic reanalysis product to further examine the features of the zonal velocity at middepth and its phase relationship with the surface wind forcing at semiannual periods in the EIO. The remainder of the paper is organized as follows: the data, methods, and reanalysis validation are described in section 2, the results and dynamical interpretation are described in section 3, and a summary and discussion are presented in section 4.

2. Data, Methods, and Evaluation

2.1. Data

We use monthly averaged zonal velocity obtained from upward looking acoustic Doppler current profilers (ADCPs) moored at 0°, 90°E (Figure 1a), from which data were collected as part of the Research Moored Array for African-Asian-Australian Monsoon Analysis and Prediction (RAMA; McPhaden et al., 2009). The ADCPs are mounted on a subsurface float, observing variations at depths between the approximately 30–40 and 350 m. The vertical resolution of the observed velocity is 10 m, and the temporal revolution is hourly. The current data are averaged monthly to obtain velocity profiles. Here we use records down to 300 m to evaluate the reanalysis product.
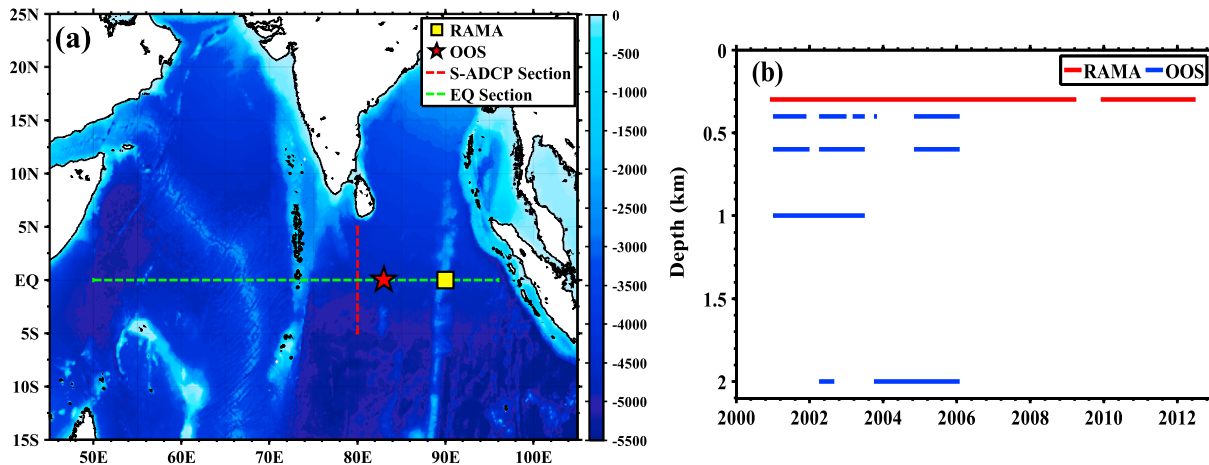
Figure 1. (a) Locations of the mooring sites deployed by RAMA at 0°, 90°E and OOS at 0°, 83°E. The blue shading indicates bathymetry. Red dotted line is the 80°E across the equator obtained from S-ADCP. Green dotted line is the selected section along equator to obtain the structure of the zonal currents. (b) Time span of the data sets used in this study. Red line represents the time series at 300 m obtained from RAMA at 0°, 90°E; blue lines represent the observed time series of OOS at 400, 600, 1,000, and 2,000 m. RAMA = Research Moored Array for African-Asian-Australian Monsoon Analysis and Prediction; OOS = Ocean Observing System; S-ADCP = shipboard acoustic Doppler current profiler.

In addition to the data from mooring at 0°, 90°E, we examine monthly zonal velocity observed from subsurface Ocean Observing System (OOS) current-meter moorings (Murty et al., 2006, 2002), which were initiated by the Ministry of Ocean Development, Government of India, and incorporated into RAMA (Figure 1a). Three OOS subsurface moorings with Recording Current Meters were deployed along the equator at 93°E, 83°E and 76°E, respectively. In the present study, we focus on the mooring at 83°E because it has the longest available records. This mooring included Recording Current Meters at five nominal depths of 200, 400, 600, 1,000, and 2,000 m between the years 2001 to 2006. Both semidiurnal and diurnal tides were removed from the time series of zonal (u) and meridional (v) current data using a 49-hr moving average. All data were monthly averaged to obtain the mean time series of u and v. The time ranges spanned by these data sets at different depths are presented in Figure 1b.

The zonal currents along the 80°E meridional section (red section in Figure 1a), collected by the 75-kHz shipboard ADCP (S-ADCP) of the South China Sea Institute of Oceanology, Chinese Academy of Sciences, research vessel SHIYAN1 during 2013 to 2014, are used to evaluate the meridional structure of the simulated middepth zonal currents. There are two quasi-synoptic cross-equatorial sections collected during 1–4 April 2013 and 25–30 April 2014. All S-ADCP measurements extend deeper than 550 m and are processed to a sampling rate of 5 min and a resolution 8 m in vertical. Before validating, the current data are linear interpolated to 0.05° spatial intervals in the latitude range from 6°S to 6°N and smoothed with a 20-point running average. The current data quality control procedures are summarized briefly in Table 1.

To help resolve the large spatial and temporal scales of the middepth currents, we also use the ocean reanalysis output obtained from the European Centre for Medium-Range Weather Forecasts (ECMWF) Ocean Reanalysis System 4 (ORAS4; Balmaseda et al., 2013; Mogensen et al., 2012) from 2000 to 2014. The ORAS4 product is generated by assimilating different observations into the version 3.0 of the Nucleus for European Modeling of the Ocean (V3.0) oceanic model (Madec, 2008), which includes temperature and salinity profiles obtained from expendable bathythermographs, conductivity-temperature-depth sensors, mooring buoys, and autonomous pinniped bathythermograph and satellite altimetry data. The model relaxes weakly (20-year time scale) to climatological salinity and temperature from the World Ocean Atlas 2005 (Antonov et al., 2006; Locarnini et al., 2006) and is forced by the atmospheric ECMWF Reanalysis (Uppala et al., 2005) from September 1957 to December 1989, and the ECMWF interim reanalysis (ERA-Interim; Dee et al., 2011) from January 1989 to December 2009 to generate the 10-day reanalysis output of ocean potential temperature, salinity, and velocity. The ORAS4 has a horizontal resolution of 1° × 1° with equatorial refinement (0.3°) and a vertical resolution of 42 levels with 24 levels below 200 m. The temporal resolution used in the present study is monthly. The timeline of ORAS4 forcing and assimilation data sets has been

Table 1
Data Quality Control and Postprocessing Procedures

Measurement	Preliminary gross automated error checking	Daily parameters that will generate error alerts	Removed semidiurnal and diurnal tides
Current meter/ADCP velocity	If daily average is based on <50% of daily samples, the output is set to undersampled flag (no data reported)	speed change greater than 50 cm/s from previous day; no change in speed from previous day;	49-hr moving average

Note. Source: Murty et al. (2006) and https://www.pmel.noaa.gov/gtmba/data-quality-control. ADCP = Acoustic Doppler Current Profilers.

summarized in Nyadjro and McPhaden (2014) and https://www.ecmwf.int/en/research/climate-reanalysis/ocean-reanalysis.

The surface wind stress is calculated using daily averages of surface wind speed data from ERA-Interim (Berrisford et al., 2011; Dee et al., 2011). The horizontal resolution of ERA-Interim wind speed is 1.5° latitude × 1.5° longitude, and it spans the period from 1 January 2000 to 31 December 2014. The magnitude of the wind stress (τ) is estimated through the wind-drag formulas, which parametrize the τ as a function of the wind speed at a certain height above the surface in the form

$$\tau = \rho_a C_d |U| U \tag{1}$$

where ρ_a is the air density (1.225 kg/m^3), C_d is the drag coefficient (1.43×10^{-3}), and U is the wind speed (Weisberg & Wang, 1997). Given the daily wind stress, we computed the monthly average output to perform the harmonic analysis as described in the next section.

2.2. Methods

To examine the wave evolution and phase propagation of middepth zonal velocity at the semiannual period in the EIO, we use harmonic analysis and complex empirical orthogonal function (C-EOF) decomposition analysis. These two methods are complementary. The harmonic analysis can efficiently isolate the target signal (semiannual variability) from the basic waves and analyze its amplitude, phase distribution, and explained variance. We also use the C-EOF approach that has advantage of extracting the principal modes of zonal velocity to estimate their propagating characteristics and amplitude in compact form. Detailed descriptions of these methods can be found in Thomson (1982) and Horel (1984).

The variability of the middepth zonal velocity in the EIO can be explained by a Boussinesq-approximation linear wave theory on the equatorial beta plane, as described in Philander (1978), Eriksen (1981), Luyten and Roemmich (1982), and Lukas and Firing (1985). This method provides a useful way to examine the vertical energy propagation associated with Kelvin waves and the long nth meridional-mode Rossby waves in the EIO. In this theory, the vertical structures are represented by the Wentzel-Kramers-Brillouin (WKB) approximation, in which the characteristic velocity c of each vertical mode is given by the estimate $c = N_b/|m|$, where N_b is the background Brünt-Väisälä frequency and m is a *local* vertical wavenumber (Gill, 1982).

2.3. ORAS4 Evaluation

To assess the ability of the reanalysis to reproduce the middepth zonal currents in the EIO, we compare the zonal velocity of the 0°, 90°E RAMA mooring and ORAS4 outputs at the depth of 300 m (Figure 2a), and the OOS data and ORAS4 outputs at 400 m (Figure 2c), 600 m (Figure 2e), 1,000 m (Figure 2g), and 2,000 m (Figure 2i) at 0°, 83°E. The results show good agreement between the observed records and the reanalysis outputs at both locations, with correlation coefficients exceeding 0.5 at all depths (significant at the 99% level). The root-mean-square difference of the reanalysis relative to the observations is 6.8 cm/s at 300 m, 7.6 cm/s at 400 m, 10.1 cm/s at 600 m, 9.1 cm/s at 1,000 m, and 5.0 cm/s at 2,000 m. Table 2 illustrates more details of statistical characteristic between the reanalysis and observations at different depths.

Evaluations of mean seasonal cycle of zonal velocity from RAMA, OOS, and ORAS4 show that there is a pronounced semiannual cycle as a function of depth. Agreement in amplitude and phase is best at 300 and 400 m between the observations and ORAS4 (Figures 2b and 2d). Agreement in phase is better than that in amplitude at 600 and 1,000 m (Figures 2f and 2h), while agreement is poor at 2,000 m (Figure 2j). Discrepancies in the comparisons at 1,000 and 2,000 m may be due to the fact that the observations span a relatively short period of time at these depths. Nevertheless, the good agreement as measured by the
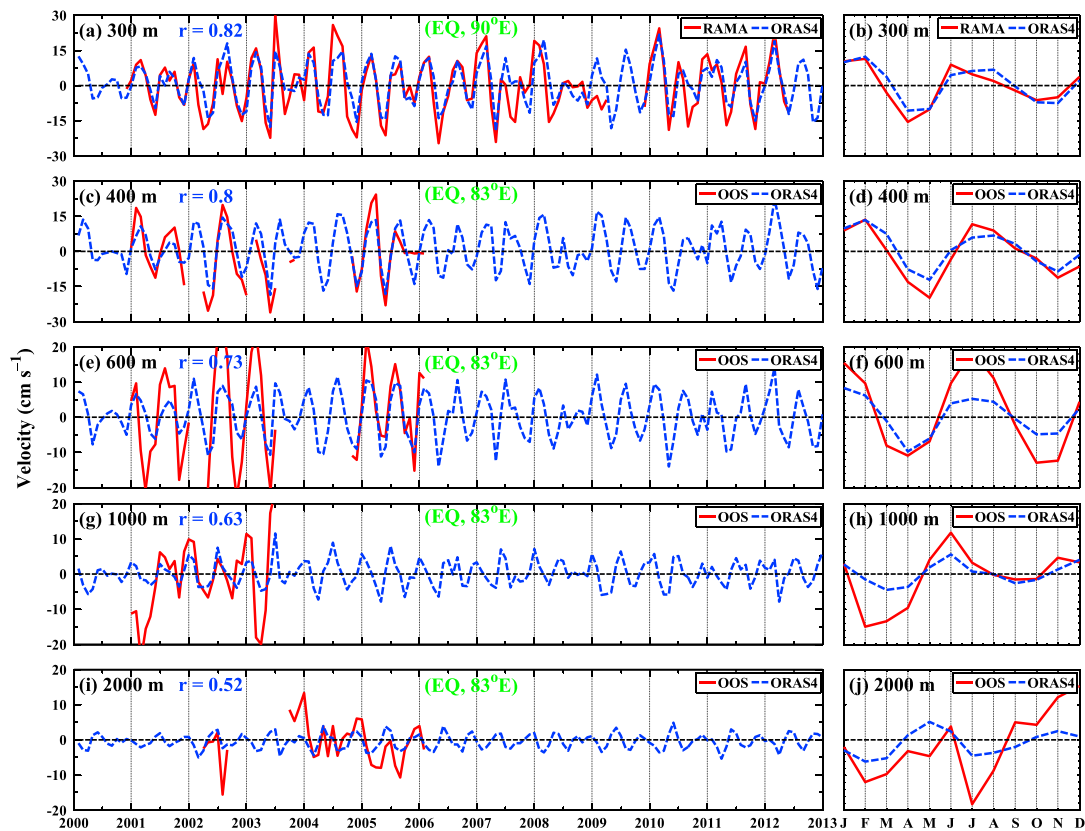
Figure 2. Comparison of the (a) whole time series and (b) mean seasonal cycle of the 300-m zonal currents (cm/s) obtained from RAMA (solid red line) and ORAS4 (dashed blue line) at 0°, 90°E. The correlation coefficient is indicated as blue numbers. (c, d) as in (a) and (b) but for the 400-m zonal currents at 0°, 83°E obtained from OOS (solid red line) and ORAS4 (dashed blue line). (e, f) As in (a) and (b) but for the 600-m zonal currents. (g, h) As in (a) and (b) but for the 1,000-m zonal currents. (i, j) As in (a) and (b) but for the 2,000-m zonal currents. RAMA = Research Moored Array for African-Asian-Australian Monsoon Analysis and Prediction; ORAS4 = Ocean Reanalysis System 4.

cross correlations and standard deviation at depths down to 1,000 m provides confidence in the ability of the ORAS4 to reproduce the large-scale variability of the middepth zonal currents.

The zonal currents from S-ADCP and ORAS4 for April 2013 and April to May 2014 display a similar latitudinal structure (Figure 3). Note that the observed two zonal velocity structures across the equator were obtained from the same single section but for different years (namely, 1–4 April 2013 and 25–30 April 2014, respectively). The observations and reanalysis output suggest that (1) the strong eastward currents occurred at upper layer (0–160 m) between 5°S and 5°N during April and (2) the westward currents below 200 m are equatorially trapped within ~3° of the north/south equator with comparable magnitudes (Figure 3c). Although the present available observations are still too sparse to draw robust conclusions regarding the meridional structure, these results suggest that ORAS4 is able to capture the equatorial trapped structure of middepth currents and their phase reversal with depth in our study region. More comparisons are discussed in the next subsection to interpret the observed features.

Table 2
Comparison of the Time Series Obtained From ORAS4 and Observations (RAMA/OOS) at Different Depths

Depth	300 m	400 m	600 m	1,000 m	2,000 m
Correlation coefficient (CORR)	0.82 (99%)[a]	0.8 (99%)	0.73 (99%)	0.63 (99%)	0.52 (99%)
Standard deviation (STD)	11.8 (RAMA)	12.3 (OOS)	14.0 (OOS)	11.0 (OOS)	5.9 (OOS)
	9.1 (ORAS4)	9.1 (ORAS4)	6.7 (ORAS4)	3.8 (ORAS4)	2.3 (ORAS4)
Root-mean-square difference (RMSD)	6.8	7.6	10.1	9.1	5.0

[a]Significant level of correlation coefficient. ORAS4 = Ocean Reanalysis System 4; RAMA = Research Moored Array for African-Asian-Australian Monsoon Analysis and Prediction; OOS = Ocean Observing System.
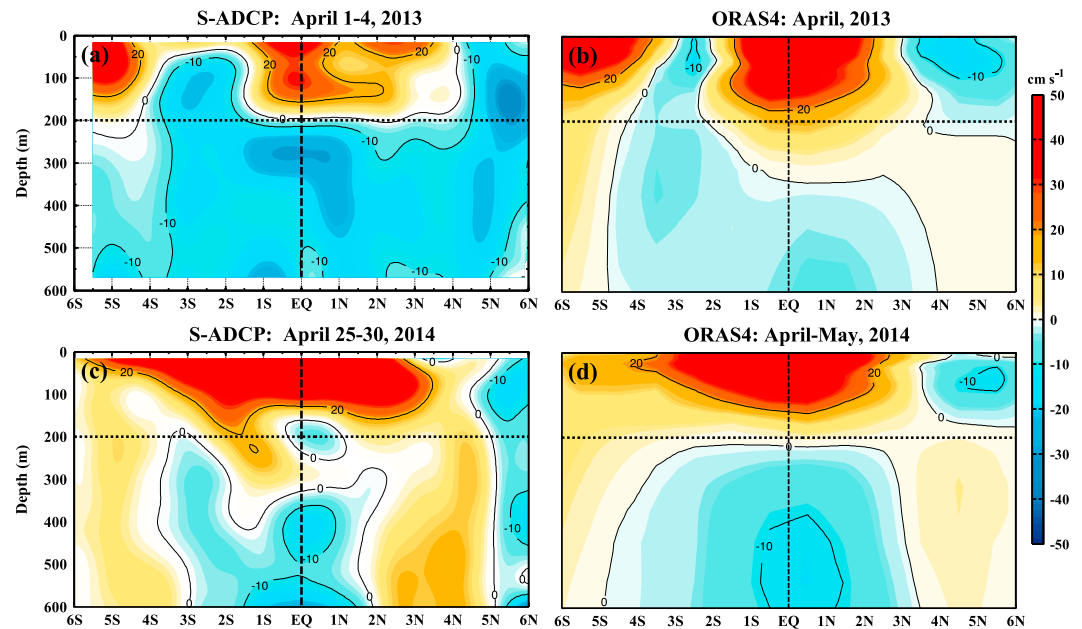
Figure 3. Comparison of the zonal currents along 80°E obtained from S-ADCP observations and the ORAS4 reanalysis. (a, c) The zonal velocities derived from S-ADCP during 1–4 April 2013 and 25–30 April 2014, respectively. (b, d) Derived from the ORAS4 during April 2013 and April–May 2014, respectively. S-ADCP = shipboard acoustic Doppler current profiler; ORAS4 = Ocean Reanalysis System 4.

3. Results

3.1. Vertical Phase Propagation of the Middepth Zonal Currents

3.1.1. Observations

We first examine the temporal variations of the climatological zonal velocity profiles obtained from OOS at 0°, 83°E (Figure 4a). The observed currents near 200 m are eastward in mid-January to early April and July to early October and westward in mid-April to June and mid-October to December, indicating a pronounced semiannual cycle (Figure 4a). Semiannual cycles are also evident at 400, 600, 1,000, and 2,000 m; however, the phases of the zonal velocities at these depths are markedly different. Results show that the eastward velocities occur near 1,000 m in October–January and May–July and near 2,000 m from mid-August to December. The semiannual variability at 2,000 m leads the observed cycles above it, revealing a clear upward phase propagation.

3.1.2. Reanalysis

Results of the middepth currents obtained from reanalysis compare well with those from the moored observations, displaying significant semiannual variability with similar vertical phase propagation (Figure 4b). The variations at deeper depths lead those above, which is a clear indication of vertical phase propagation. However, there are noticeable differences in the maximum velocity and phase speed of the middepth currents compared with the observations, with the reanalysis tending to have stronger upward phase propagation in some months. These differences might be attributed to coarse vertical resolution of the OOS observations and/or the limited availability of data at 1,000- and 2,000-m depth (Figures 2e and 2g). Additionally, the differences in stratification between the ORAS4 and moored observation could also affect the comparison.

Focusing on ORAS4, the basin-scale variations in middepth zonal currents along the equator exhibits a predominantly semiannual cycle with upward phase propagation (Figure 5). A period of westward flow occurs initially below 1,200 m in the eastern basin in January, propagating upward and westward, and fully occupying the central basin in April, and finally covering only a small fraction of the upper western corner of the basin in August. With the period of westward flow ending, eastward flow initially occurs in April, peaks in August, and ends in November. These results are consistent with and further expand the observed results at 0°, 83°E by demonstrating that across the basin, zonal currents at deeper depths along the equator lead currents at the shallower depths, with a clear upward phase propagation.
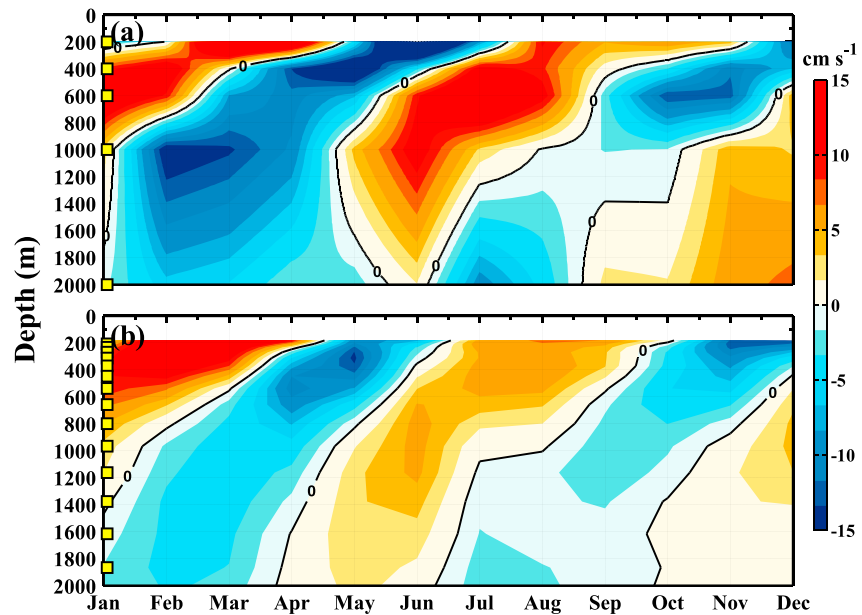
Figure 4. (a) Time-depth plot of the observed climatological monthly mean zonal currents at 0°, 83°E. The yellow squares on the vertical axes indicate the various observed depths of 200, 400, 600, 1,000, and 2,000 m. The vertical profiles are linear interpolated into 10-m intervals. (b) As in (a) but for the Ocean Reanalysis System 4 reanalysis.
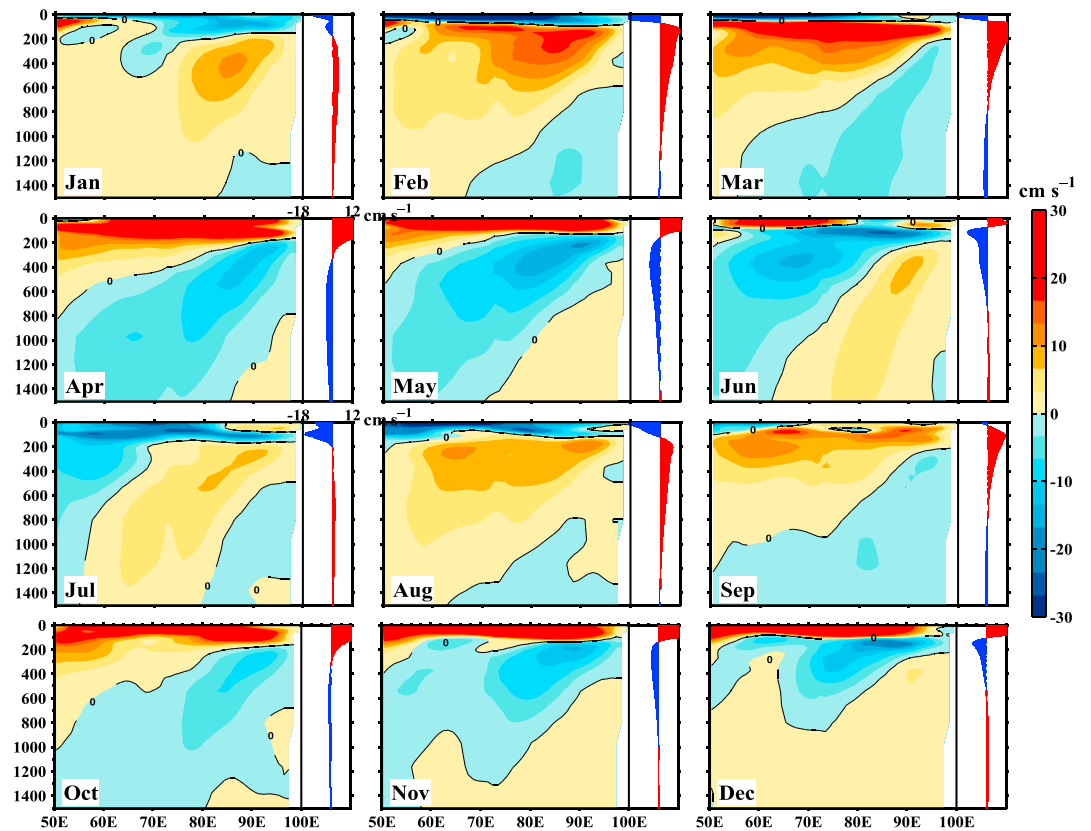

Figure 5. Longitude-depth plots of the climatological zonal currents along the equator averaged over 0.5–0.5°N, derived from Ocean Reanalysis System 4 (2000–2014). Black lines represent the zero velocity contours. On the right of each panel, the zonal average of the zonal currents is shown in a vertical profile, with the mean eastward and westward currents in red and blue, respectively.
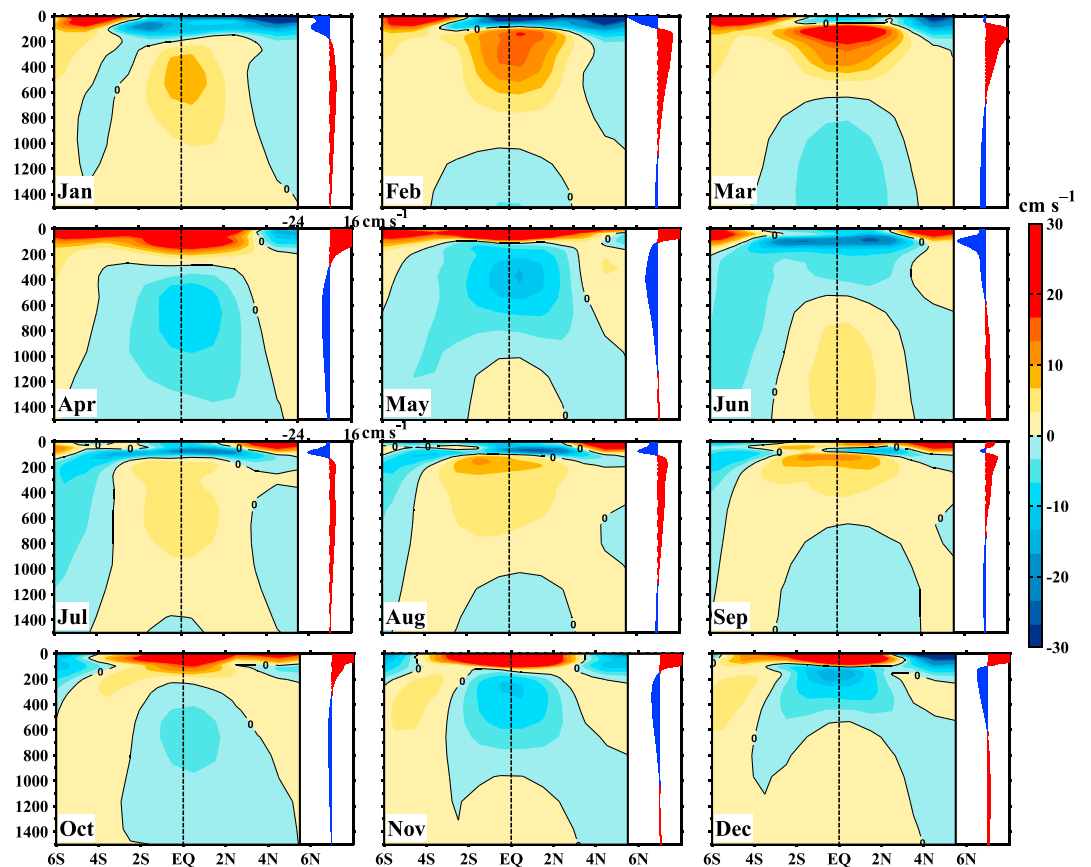
Figure 6. Latitude-depth plots of the climatological zonal currents averaged over 79.5–80.5°E, derived from Ocean Reanalysis System 4 (2000–2014). Black lines represent the zero velocity contours. On the right of each panel, the meridional average (3°S to 3°N) of the zonal currents is shown in vertical profiles, with the mean eastward and westward currents in red and blue, respectively.

The most prominent feature of the zonal currents that span the equator along the 80°E section in ORAS4 is that the middepth velocities are equatorially trapped with a vertical propagating phase on the equator (Figure 6). Generally, the monthly variability of middepth zonal flows near the equator is bordered to the north and south by oppositely directed currents centered near 4°–6°N and 4°–6°S. All these features suggest that the equatorially trapped, semiannual phase reversals and vertical phase propagation of middepth zonal currents are the manifestation of low-frequency wind-driven equatorial linear waves (Dengler & Quadfasel, 2002; Kessler & McCreary, 1993; Luyten & Roemmich, 1982). In the next section, we isolate the semiannual signals from the original zonal velocity to discuss the mechanisms responsible for the vertical propagation and equatorial trapped structures in the ORAS4 ocean reanalysis product.

3.2. Mechanisms of Vertical Propagation
3.2.1. Evidence for Vertically Propagating Semiannual Rossby Waves

To investigate the dynamics of these middepth zonal currents, we analyze longitude-depth variations of amplitude, phase, and explained variance of the semiannual harmonic in zonal velocity along the equator obtained from ORAS4 (Figure 7). The results identify two distinct regions of elevated wave energy:

1. Above 150 m from 50°E to approximately 80°E, the semiannual harmonic explains 50–70% of the variance of the total zonal currents with an amplitude greater than 20 cm/s (Figure 7) that is related to the surface wind forcing in the EIO (see Figure 14 and Han et al., 1999; Nagura & McPhaden, 2016).
2. Beneath the pycnocline, a *bright zone* extends from 97°E and a depth of 200 m to approximately 70°E and a depth of 1,500 m, explaining 50–75% of the variance of the semiannual harmonic with an amplitude
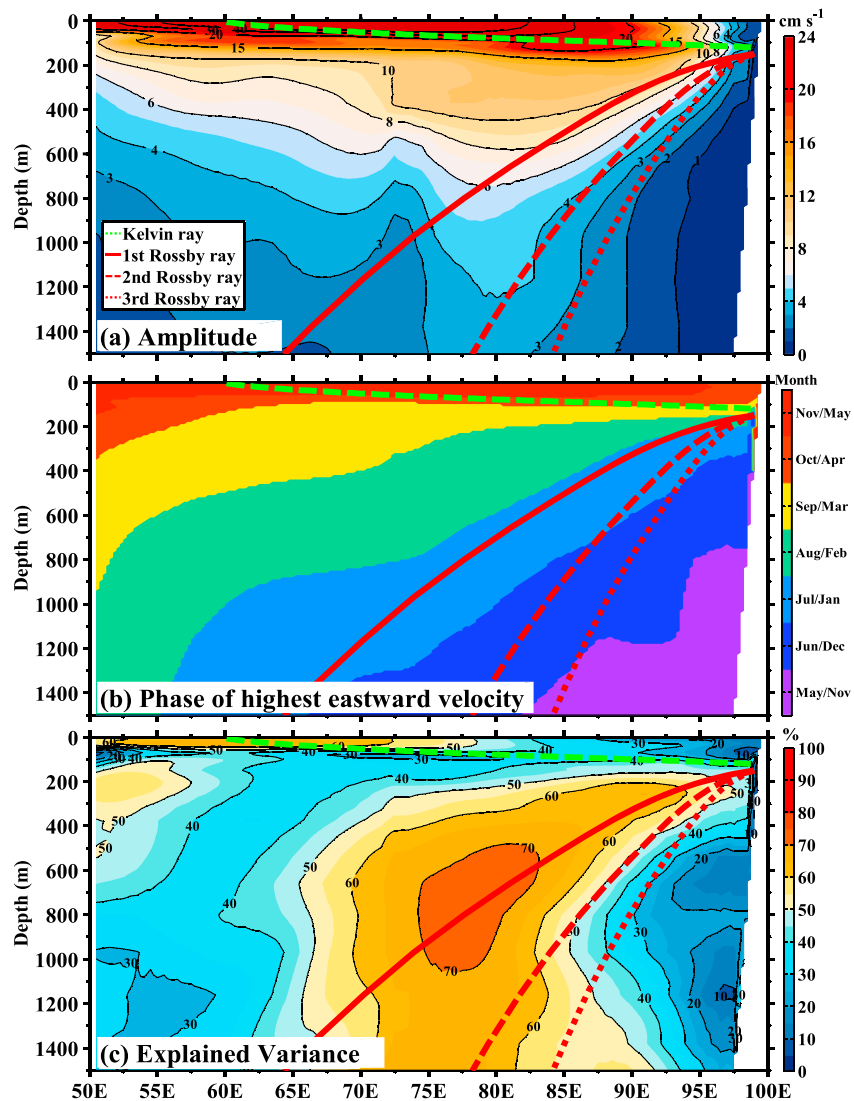
Figure 7. Semiannual harmonic of the monthly zonal velocities along the equator obtained from Ocean Reanalysis System 4 (2000–2014): (a) Amplitude (cm/s), (b) phase (month), and (c) percentage of the explained variance (%). The phase is defined as the month of the strongest westward velocity. The energy ray of the theoretical Wentzel-Kramers-Brillouin waves is also shown as follows: wind-generated Kelvin waves (green dashed lines) and reflected Rossby waves of the first (red solid lines), second (red dashed line) and third (red dotted line) meridional modes. The slopes are calculated using $-\omega_0/N_b(z)$ for the Kelvin wave and $(2n + 1)\,\omega_0/N_b(z)$ for the nth meridional-mode Rossby wave, where ω_0 denotes the semiannual frequency (180-day period) and $N_b(z)$ the background Brünt-Väisälä frequency profile (based on the N of the reanalysis averaged along the equator).

greater than 3 cm/s (Figure 7). In addition, a *shadow zone* occurs at middepths in the eastern and western basins, where the amplitude and percentage of explained variance for the semiannual harmonic are greatly diminished.

The Kelvin wave raypath for the semiannual harmonic (Figure 7a) propagates downward and eastward in the upper 200 m (Han et al., 1999; Nagura & McPhaden, 2016). On reaching the eastern boundary, it reflects into Rossby waves that propagate westward into the deep ocean. The region with large explained variance progressively thickens from the east toward the west and extends to greater depths in the central Indian Ocean (Figure 7c). The phase lines are approximately parallel, with phase propagating upward and westward (Figure 7b), consistent with linear wave theory for long equatorial Rossby waves. The upward phase propagation indicates downward energy propagation as the waves progress to the west.
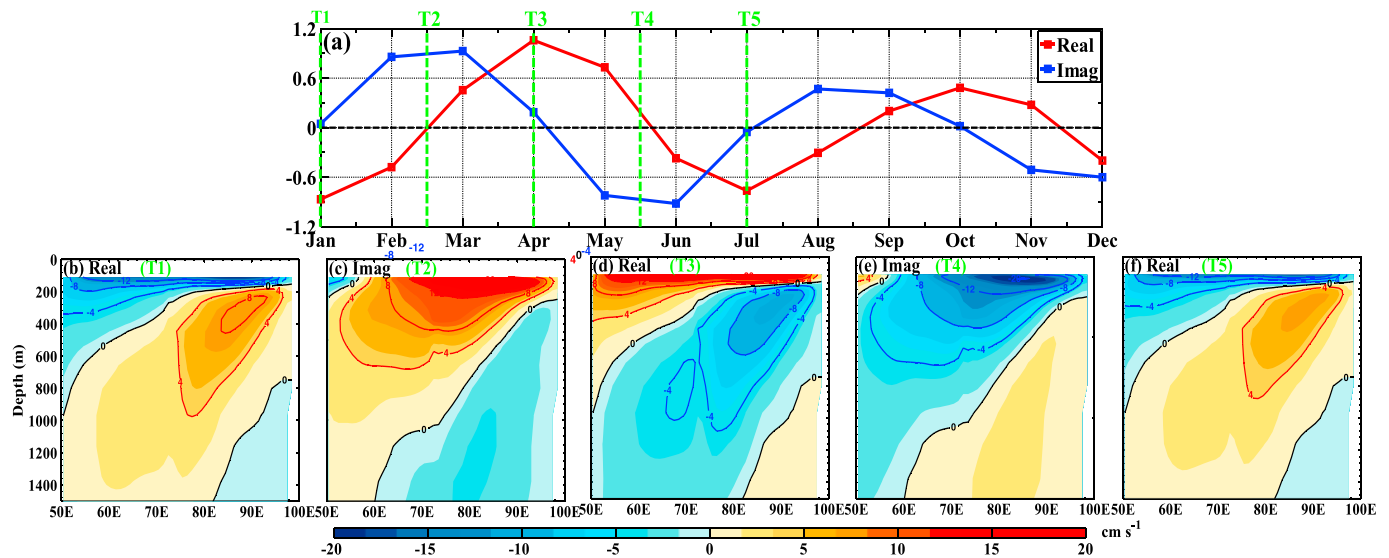
Figure 8. Temporal and spatial evolution of the first complex empirical orthogonal function mode obtained from the monthly zonal velocities of Ocean Reanalysis System 4 between 2000 and 2014 along the equator: (a) temporal evolution of the climatological principal components; red line represents the real part and blue the imaginary part; (b–f) spatial evolution of the real and imaginary parts consistent with the principal components. The green dotted lines in (a) represent the selected month corresponding to the spatial evolution of the complex empirical orthogonal function in (b)–(f).

According to WKB theory for nondispersive equatorial waves, phase isolines are approximately parallel to the raypaths (i.e., direction of phase speed is perpendicular to group speed). The raypath of the first-meridional-mode Rossby mode is parallel to the phase lines in the basin interior (Figure 7b), while that of the second- and third-meridional-mode Rossby waves slope more rapidly into the middepth ocean than the first mode. Therefore, we infer that the second and third modes do not contribute as significantly as the first mode to middepth zonal current variability in the ocean basin interior. The zonal and vertical differences of phase lines in Figure 7b can be used to roughly estimate the propagating wavelength of the equatorial long waves in the equatorial section. Results indicate an average zonal wavelength of about 7,000 km in the eastern basin and about 15,000 km in the western basin, together with a vertical wavelength in the range of about 2,000 to 4,500 m. These solutions are approximately in agreement with linear equatorial theory of low-frequency long waves, supporting the downward propagation of the long Rossby waves at semiannual periods, emanating from the eastern boundary of the EIO to affect middepth zonal current variability.

Results from the C-EOF decomposition further document the evolution of the vertically propagating semi-annual waves at middepths in the EIO. The temporal and spatial patterns (including the real and imaginary parts) of the first C-EOF mode (68.6% explained variance) confirm these propagating features of middepth zonal currents (Figure 8). The zonal wavelength of the propagating waves at middepths is estimated as twice the distance between the two zero crossings in the real or imaginary signals. That wavelength yields a zonal phase velocity of approximately 0.57 m/s, which implies that it takes about 4.5 months for a wave to cross the basin along the equator. The amplitude and phase of the spatial patterns obtained from the real and imaginary parts of the first C-EOF are also calculated (Figure 9), which are consistent with the esti-mated amplitude and phase of the semiannual harmonic fit (Figures 7a and 7b). These results support the interpretation of our results in terms of vertically propagating Rossby waves at semiannual periods in the EIO.

3.2.2. Evidence for Meridionally Trapped Equatorial Waves

To address the meridional structure of the middepth zonal currents, we examine the amplitude, phase, and explained variance of the semiannual harmonic in a meridional section at 80°E (Figure 10). The spatial struc-ture of the phase is typically homogeneous across all latitudes between 3°S and 3°N, with phase lines approxi-mately horizontal across the equator and upward phase propagation with a vertical wavelength of about 2,000 m (Figure 10b). The maximum amplitude and explained variance occur in the equatorial band between about 3°N and 3°S (Figures 10a and 10c), with the amplitude close to the original velocities, suggesting that the overwhelming response of the middepth currents in the tropical ocean is semiannual. At semiannual
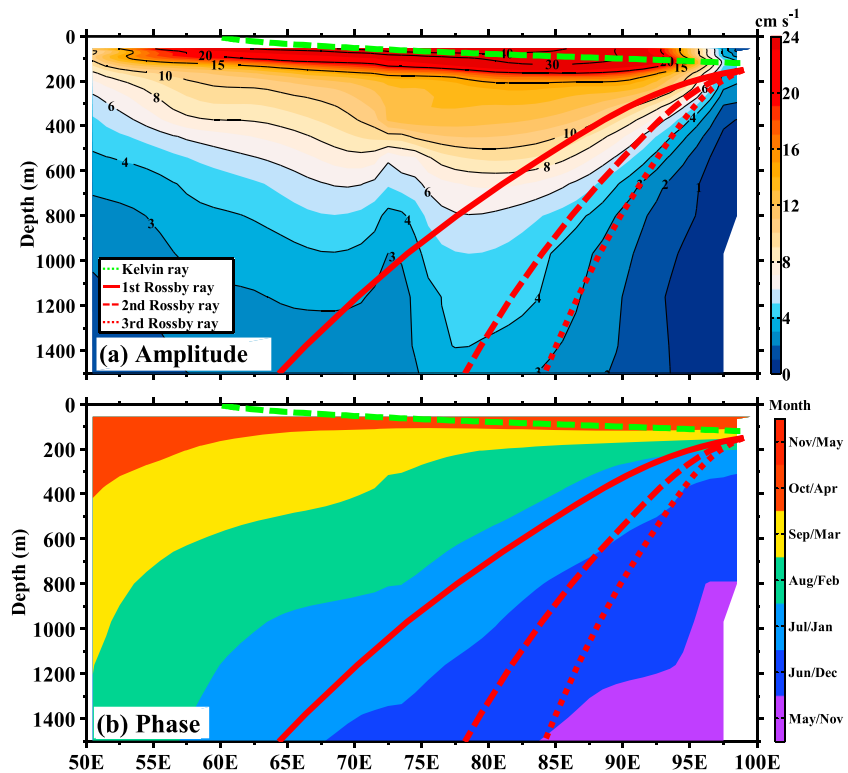
Figure 9. (a) Amplitude and (b) phase of the spatial patterns obtained from the real and imaginary parts of the first complex empirical orthogonal function. The amplitude is derived from the square root of the sum of the squares of the real and imaginary spatial patterns. The phase is derived from the inverse tangent of the quotient of the real and imaginary spatial patterns. The energy ray of the theoretical Wentzel-Kramers-Brillouin waves is shown as in Figure 7.

periods, the highest eastward velocities in the equator occur in June at 1,400 m, propagating upward to 250 m in September. Velocities off the equator weaken poleward (Figure 10a) and reverse abruptly compared to the flow at the equator, leading approximately three months with the equatorial currents in nearly 4°N/S off the equator (Figure 10b). This seesaw pattern of meridional structure and vertical propagation is in large part compatible with the first-meridional-mode Rossby wave at semiannual periods generated by Kelvin reflection at the eastern boundary.

3.2.3. Interpretation as Equatorial Propagating Linear Waves

The above basic findings of the equatorial middepth zonal currents are quantitatively interpreted in terms of the WKB theory for linear waves on the equatorial β plane. This theory allows us to assess the features of equatorial waves in terms of the dispersion relation and meridional modes (Luyten & Roemmich, 1982). Figure 11a shows the vertical profile of Brünt-Väisälä Frequency (mean $N = 4.3 \times 10^{-3}$ s^{-1}) for calculating the dispersion relation and Figure 11b presents the calculated dispersion curves of vertical wavenumber (m) versus zonal wavenumber (k) at $\omega = 4\pi$ year^{-1} for the Kelvin wave and for the first three nondispersive Rossby waves. Here we focus on the waves where the amplitude and variance explained are largest, namely, 70–85°E, 500–1,000 m, with the zonal and vertical wavelengths in this region derived from the phase structure of the semiannual harmonic in Figure 7b.

The green symbol x in Figure 11b represents the estimate of mean zonal and vertical wavenumber in the focus region ($k = -2\pi/10,300$ km and $m = 2\pi/2,600$ m, respectively), with the green rectangular box showing the estimated uncertainty about this estimate. The dispersion curve of $n = 1$ meridional-mode Rossby wave is close to the green symbol x and fully encompasses the estimated box, confirming that the first-meridional-mode Rossby wave is the primary cause for the variability of middepth zonal current. This result also indicates the absence of the energy for second- and third-meridional-mode Rossby waves and Kelvin wave over the focus region. Note that the dispersion curve of the second-meridional-mode Rossby wave also crosses a small part of estimated box; however, this Rossby wave in theory has zero zonal velocity on the equator (Figure 12f) and makes no contribution to the middepth zonal velocity there. In addition to the waves described above,
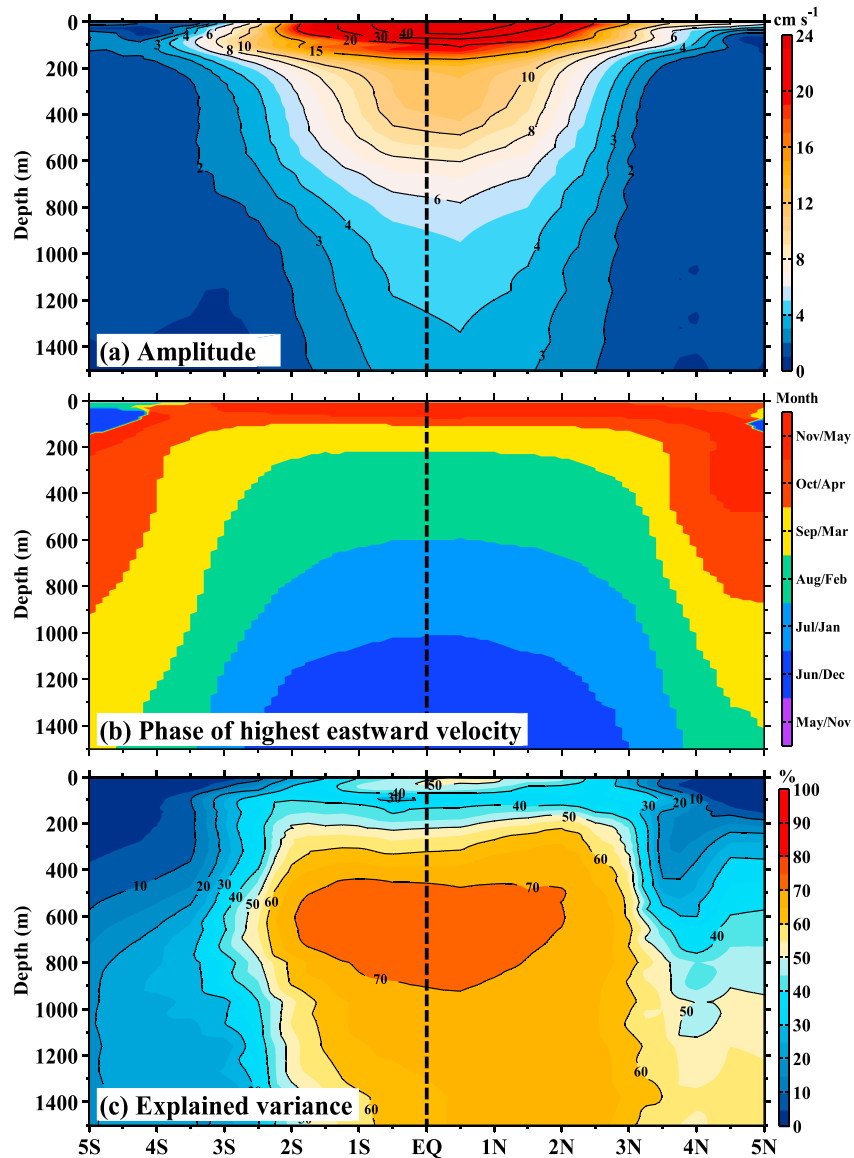
Figure 10. As in Figure 7 but for the meridional section at 80°E.

the full dispersion relation of the linear equatorial motion equation also has a mixed Rossby-gravity wave ($n = 0$) at low frequency, corresponding to a set of short Rossby waves. We are not able to detect this dispersive wave in the present study because of our emphasis on large zonal scale features in middepth zonal velocity.

Given the zonal wavenumber, the vertical wavenumber, and frequency for an equatorial wave, we can relate the meridional structure of observed zonal velocity in the reanalysis to that expected from the theory for equatorial Rossby waves. For a detailed theoretical description of meridional structure of equatorial waves, the reader could be referred to Matsuno (1966), Moore and Philander (1977), and Eriksen (1980). Here we only introduce aspects that are essential for our discussion. The Rossby wave zonal velocity in a linear Boussinesq ocean for unforced inviscid incompressible rotating flow on an equatorial β plane is as follows:

$$U_n(\eta) = A_n \left[-\frac{\left(\frac{n}{2}\right)^{1/2} \psi_{n-1}}{\sigma + s} - \frac{\left(\frac{n+1}{2}\right)^{1/2} \psi_{n+1}}{\sigma - s} \right] \cdots (n = 1, 2, \ldots,) \tag{2}$$

where A_n is amplitude, here given $A_n = 1$. The symbols η, σ, and s are the nondimensional latitude, frequency, and zonal wavenumber given as follows:
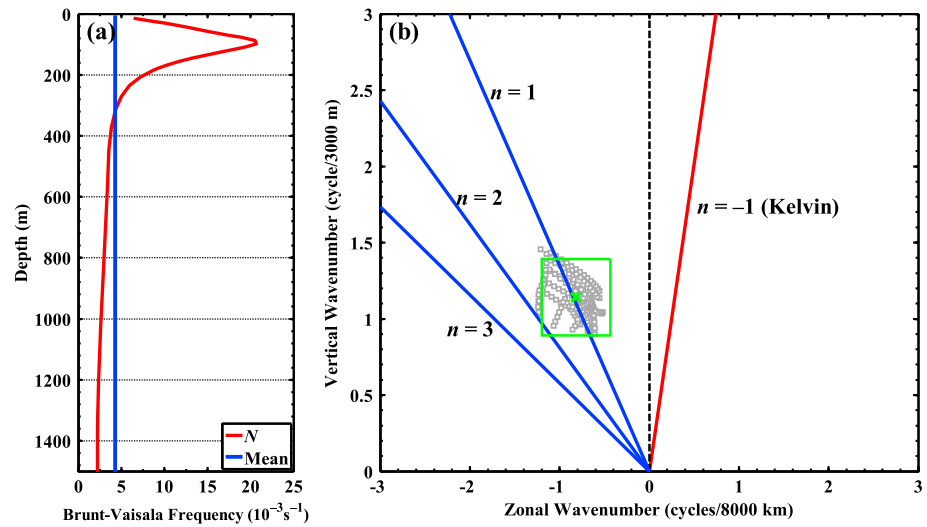
Figure 11. (a) The vertical profile of Brünt-Väisälä frequency (*N*) averaged along the equator (red line) and its mean (blue line). (b) Dispersion diagram of the vertical wavenumber versus the zonal wavenumber at $\omega = 4\pi$ year^{-1} for $N = 4.3 \times 10^{-3}$ s^{-1}. The green symbol x represents the estimated mean values from the equatorial region where the amplitude and variance explained are largest, namely, 70–85°E, 500–1,000 m. The green box shows the uncertainties of 95% confidence (twice the standard deviation). The gray squares are the estimated values from the focus region.

$$\eta = (\beta/c)^{1/2}y \quad \sigma = \omega/(\beta c)^{1/2} \quad s = (c/\beta)^{1/2}k \tag{3}$$

ψ_n is a Hermite function given as follows:
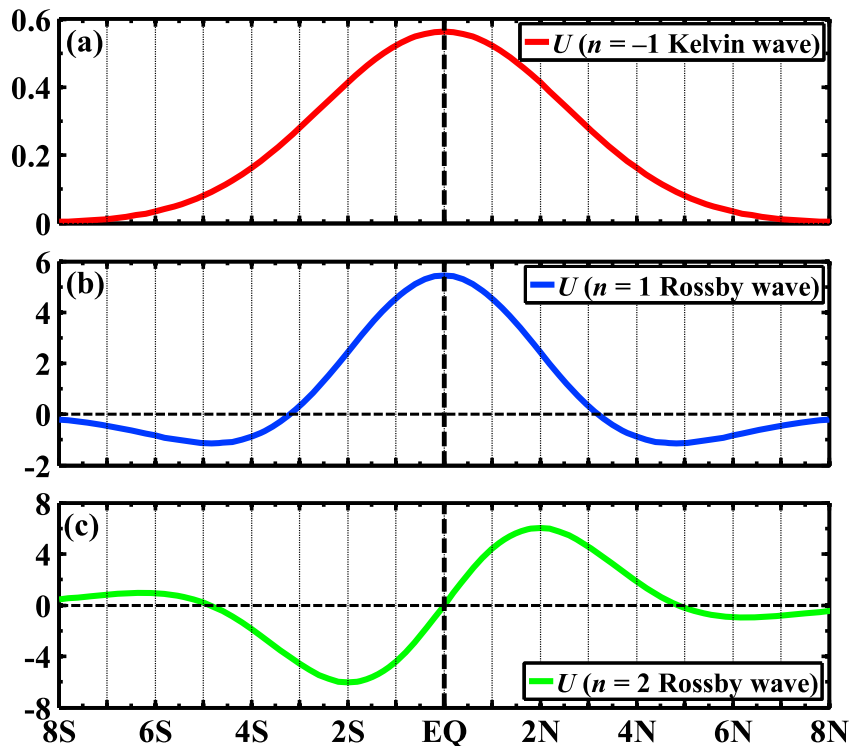
Figure 12. Theoretical meridional distribution of zonal velocity of (a) Kelvin wave and (b) first- and (c) second-meridional-mode Rossby waves at semiannual periods obtained from equations (1) and (4), respectively.
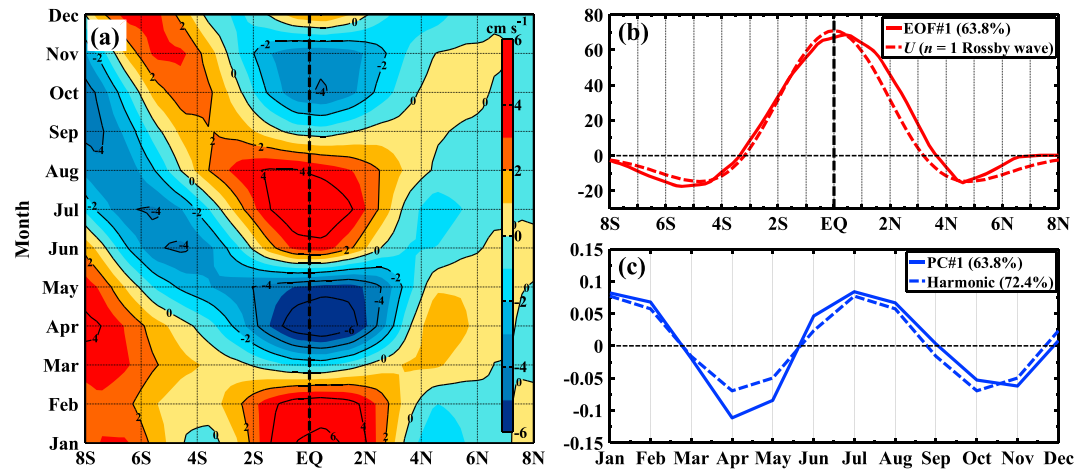
Figure 13. (a) The meridional distribution of climatological (2000–2014) monthly ORAS4 zonal velocity along 80°E averaged between 500 and 1,000 m. (b) The spatial mode of first EOF of the monthly ORAS4 zonal velocity along 80°E averaged between 500 and 1,000 m during 2000 and 2014 (red solid line) and the theoretical meridional distribution of zonal velocity of first-meridional-mode Rossby wave (red dashed line). Blue solid line in (c) is the same as in (b) but for the principal component of first EOF. Blue dashed line in (c) is the semiannual harmonic of the monthly ORAS4 zonal velocities at the equator averaged between 500 and 1,000 m during 2000 and 2014. ORAS4 = Ocean Reanalysis System 4; EOF = empirical orthogonal function.

$$\psi_n(\eta) = \frac{e^{-\eta^2/2} H_n(\eta)}{(2^n g n! \pi)^{1/2}} \tag{4}$$

where $H_n(\eta)$ are the Hermite polynomials, with the first few Hermite polynomials being $H_0(\eta) = 1$, $H_1(\eta) = 2\eta$, $H_2(\eta) = 4\eta^2 - 2$, $H_3(\eta) = 8\eta^3 - 12\eta$. The symbol y is the distance in meridional direction. The eigenvalues $c = N_b/|m| = 1.78$ m/s describes the characteristic speed. To complement the meridional structure of the Rossby waves, we further analyze the meridional structure of the semiannual equatorial Kelvin wave, of which the wave function is as follows:

$$U_{-1}(\eta) = A_{-1}\psi_0 \tag{5}$$

Results from Figure 12 show that theoretical Rossby waves at semiannual time scales have a complicated meridional structure with reversals in phase of zonal velocity at various latitudes depending on the meridional mode number. For $n = 1$ mode, the zonal velocity is symmetric about the equator with the strongest zonal motion at the equator and the trapped structure within 3° of the equator (Figure 12b), while for $n = 2$ mode, the zonal velocity is antisymmetric with no zonal motion at the equator (Figure 12c). Due to the observed symmetry of zonal velocity about the equator (Figure 3), only the first-meridional-mode Rossby wave is consistent with the S-ADCP observations on the equator. For the Kelvin wave (Figure 12a), it has a unidirectional meridional distribution of zonal velocity about the equator for a given vertical wavenumber, which conflicts with the observed reversal of middepth zonal flow at 2–3° off the equator.

The meridional distribution of zonal velocity for the first-meridional-mode nondispersive Rossby wave predicted by linear theory agrees well with the results of ORAS4 reanalysis (Figure 13). The zonal velocity obtained from ORAS4 reverses at about 3° off the equator (Figure 13a), which can account for the phase reversal of the zonal flow from the first mode of EOF decomposition (EOF1, Figure 13b). Note that this EOF1 explains 63.8% of the total variance of the zonal velocity at this section, with a dominant semiannual cycle that correspondence with the semiannual harmonic result (Figure 13c). These results indicate that the oppositely directed motions to the north and south equator with prominent semiannual period that are captured in the observations and reanalysis are dominated by the symmetric structure of the first-meridional-mode Rossby wave.

3.2.4. Forcing of the Semiannual Vertically Propagating Waves

In this section we focus on the role of the semiannual wind forcing in causing the vertically propagating semiannual Kelvin waves and reflected Rossby waves at middepth. Figure 14 presents the amplitude, phase, and
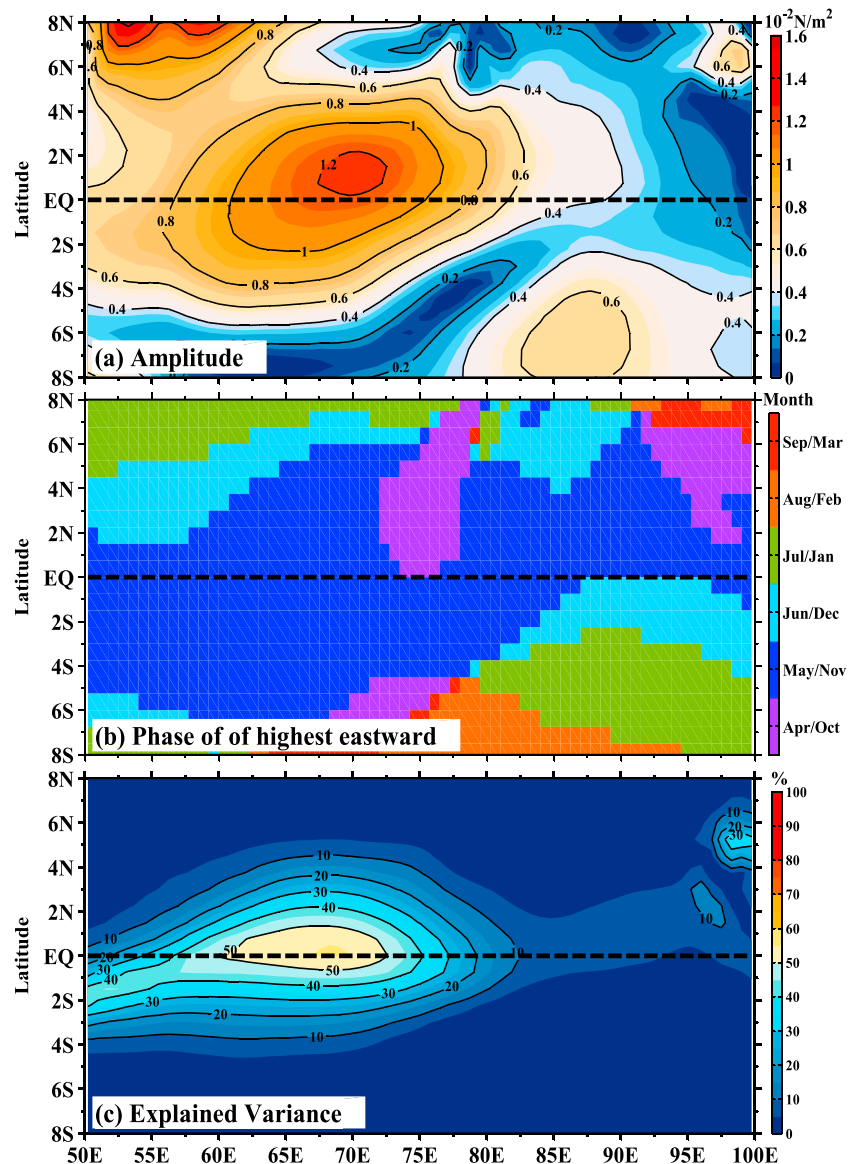
Figure 14. Spatial distribution of the semiannual harmonic for the monthly zonal wind stress derived from ERA-Interim (2000–2014): (a) amplitude, (b) phase of the highest eastward wind stress (month), and (c) percentage of the explained variance (%).

explained variance of the semiannual harmonic for the zonal component of the ERA-Interim wind stress (used to force the model). As previously described (Han et al., 1999; Nagura & McPhaden, 2016; Yamagata et al., 1996), the semiannual component of the zonal wind stress above the EIO consists of two distinct signals:

1. Along the equator, the amplitude of the semiannual variability in the zonal wind stress is greater in the western and central basins than in the eastern basin (Figure 14a), with a maximum amplitude of 1.2×10^{-2} N/m^2, contributing over 50% of the variance. The maximum eastward wind stress occurs twice a year, in boreal May and November.

2. Away from the equator, there is weak semiannual variability with a small amplitude that explains less than 20% of the total variance.

The phase of the eastward zonal wind stress (Figure 14b) agrees well with that of the surface zonal current velocities (maximum eastward current velocity in May/November, Figure 7b) as described by Nagura and McPhaden (2010, 2016). This suggests that the semiannual variability in surface zonal velocity is strongly forced by the pronounced zonal wind stress in the western EIO and that this wind stress forcing is the

likely energy source for an equatorial Kelvin wave (Figure 7), which propagates downward to the east into the pycnocline of the eastern basin (Nagura & McPhaden, 2016). These wind-forced Kelvin waves hit the eastern boundary and are reflected back into the interior as boundary-generated westward radiating Rossby waves, which propagate energy downward and phase upward at middepths, consistent with linear equatorial wave theory (McCreary, 1984).

4. Summary and Discussion

In this study, the vertical phase propagation of middepth zonal currents and their relationship with surface wind forcing in the EIO are investigated based on in situ velocity observations obtained from moorings along the equator (83°E and 90°E) in the eastern Indian Ocean and the ORAS4 reanalysis velocity output. We focus on the hypothesis that wind-forced Kelvin waves reflect into vertically propagating Rossby waves, which contribute greatly to observed semiannual variability in middepth zonal currents. We use the available current-meter observations to examine mean seasonal cycles of zonal velocity at 83°E based on the moored records at 200, 400, 600, 1,000, and 2,000 m for the years 2001 to 2006. The observations exhibit a pronounced semiannual cycle that indicates upward phase propagation. To further examine this upward phase propagation, we use ORAS4 reanalysis velocities at 0°, 83°E and 0°, 90°E during the same times as the moored observations. The results compare well for the full time series and for the semiannual cycle, which indicates that the reanalysis output and in situ observations produce consistent results.

We investigate the vertical propagation of the middepth zonal currents by analyzing the monthly evolution of the zonal velocity along the equator and the meridional section along 80°E using ORAS4. The phase reversals from eastward to westward velocity in May and November at middepth along the equator indicate strong semiannual variability. The propagating signals occur initially in the eastern basin and then, over the course of six months, move upward and westward into the western basin. This upward propagation is equatorially trapped and does not extend poleward of 3° in either hemisphere.

We expand the results of Luyten and Roemmich (1982) to the whole EIO basin and interpret the vertical phase propagation of the middepth zonal currents based on linear equatorial wave theory. The wave trajectories calculated based on the WKB approximation suggest that the vertical propagation at middepths in the ocean at semiannual periods is dominated by first-meridional-mode Rossby waves. These waves are generated by the reflection of the Kelvin wave at the eastern boundary then propagate phase upward and westward and energy downward. Semiannual harmonics of the zonal wind stress are used to investigate the forcing of the zonal currents at semiannual periods. Results suggest that semiannual period Kelvin waves are excited at the surface by the zonal wind stress variations in the western Indian Ocean (with the phase and phase speed matching well with those of the zonal wind stress). These Kelvin waves then reach the eastern basin and reflect as boundary-generated Rossby waves propagating back into the interior ocean. Harmonic and C-EOF analyses display similar vertically propagating phase patterns at semiannual periods for middepth zonal velocity, demonstrating the robustness of these features.

Theory suggests that in the EIO, second baroclinic mode equatorial Kelvin and long Rossby waves are in resonance with the semiannual wind forcing because of the time it takes these waves to traverse the width of the basin (Cane & Moore, 1981; Han et al., 1999, 2011; Jensen, 1993). Our harmonic analysis suggests that this second baroclinic mode resonance contributes to middepth depth variability in the central basin because the characteristic wave speed determined from our analysis ($c = N_b/|m| = 1.78$ m/s) (Gill, 1982; Luyten & Roemmich, 1982) is close to that of the second baroclinic mode ($c_2 \sim 1.67$ m/s in Han et al., 2011). Note that our analysis and interpretation ignore the effects of islands and complicated coastlines. The effects of the Maldives (Knox, 1974), for example, may distort middepth zonal currents in the EIO, but these effects are likely to be localized (Nagura & Masumoto, 2015). For long nondispersive low-frequency waves, nonuniform boundaries are not likely have a major influence on the dominate wave modes (e.g., Nagura & McPhaden, 2010) because their wavelengths are so large. Note that although the reflection efficiency of the western boundary is much lower than that of the eastern boundary in the EIO (e.g., Nagura & McPhaden, 2014), western boundary reflected waves are still very important (Han et al., 2011). The role of western boundary reflected waves in modulating the characteristics of the middepth zonal current needs further study.

References

Antonov, J. I., Locarnini, R. A., Boyer, T. P., Mishonov, A. V., & Garcia, H. E. (2006). *World Ocean atlas 2005, Vol. 2: Salinity, NOAA Atlas NESDIS* (Vol. 62, p. 182). Washington, DC: U.S. Government Printing Office.

Balmaseda, M. A., Trenberth, K. E., & Kallen, E. (2013). Distinctive climate signals in reanalysis of global ocean heat content. *Geophysical Research Letters*, *40*, 1754–1759. https://doi.org/10.1002/grl.50382

Berrisford, P., Dee, D. P., Poli, P., Brugge, R., Fielding, K., Fuentes, M., et al. (2011). *The ERA-Interim archive version 2.0*, in *ERA Report Series*, p. 23, ECMWF, Shinfield Park, Reading.

Boning, C. W., & Schott, F. A. (1993). Deep currents and the eastward salinity tongue in the equatorial Atlantic—Results from an eddype-solving, primitive equation model. *Journal of Geophysical Research*, *98*(C4), 6991–6999. https://doi.org/10.1029/92JC02815

Brandt, P., Claus, M., Greatbatch, R. J., Kopte, R., Toole, J. M., Johns, W. E., & Böning, C. W. (2016). Annual and semiannual cycle of equatorial Atlantic circulation associated with basin–mode resonance. *Journal of Physical Oceanography*, *46*(10), 3011–3029. https://doi.org/10.1175/JPO-D-15-0248.1

Brandt, P., & Eden, C. (2005). Annual cycle and interannual variability of the mid-depth tropical Atlantic Ocean. *Deep Sea Research Part I*, *52*(2), 199–219. https://doi.org/10.1016/j.dsr.2004.03.011

Cane, M. A., & Moore, D. W. (1981). A note on low-frequency equatorial basin modes. *Journal of Physical Oceanography*, *11*(11), 1578–1584. https://doi.org/10.1175/1520-0485(1981)011<1578:Anolfe>2.0.Co;2

Chen, G., Han, W., Li, Y., Wang, D., & Mcphaden, M. J. (2015). Seasonal-to-interannual time-scale dynamics of the equatorial undercurrent in the Indian Ocean. *Journal of Physical Oceanography*, *45*(6), 1532–1553. https://doi.org/10.1175/Jpo-D-14-0225.1

Dee, D. P., Uppala, S. M., Simmons, A. J., Berrisford, P., Poli, P., Kobayashi, S., et al. (2011). The ERA–Interim reanalysis: Configuration and performance of the data assimilation system. *Quarterly Journal of the Royal Meteorological Society*, *137*(656), 553–597. https://doi.org/10.1002/qj.828

Dengler, M., & Quadfasel, D. (2002). Equatorial deep jets and abyssal mixing in the Indian Ocean. *Journal of Physical Oceanography*, *32*(4), 1165–1180. https://doi.org/10.1175/1520-0485(2002)032<1165:Edjaam>2.0.Co;2

Dewitte, B., & Reverdin, G. (2000). Vertically propagating annual and interannual variability in an OGCM simulation of the tropical Pacific Ocean in 1985–94. *Journal of Physical Oceanography*, *30*(7), 1562–1581. https://doi.org/10.1175/1520-0485(2000)030<1562:VPAAIV>2.0.CO;2

Duan, Y., Liu, L., Han, G. Q., Liu, H. W., Yu, W. D., et al. (2016). Anomalous behaviors of Wyrtki Jets in the equatorial Indian Ocean during 2013. *Scientific Reports*, *6*(1), 29688. https://doi.org/10.1038/srep29688

Eriksen, C. C. (1980). Evidence for a continuous spectrum of equatorial waves in the Indian Ocean. *Journal of Geophysical Research*, *85*(C6), 3285–3303. https://doi.org/10.1029/JC085iC06p03285

Eriksen, C. C. (1981). Deep currents and their interpretation as equatorial waves in the western Pacific Ocean. *Journal of Physical Oceanography*, *11*(1), 48–70. https://doi.org/10.1175/1520-0485(1981)011<0048:Dcatia>2.0.Co;2

Firing, E. (1987). Deep zonal currents in the central equatorial Pacific. *Journal of Marine Research*, *45*(4), 791–812. https://doi.org/10.1357/002224087788327163

Fischer, J., & Schott, F. A. (1997). Seasonal transport variability of the deep western boundary current in the equatorial Atlantic. *Journal of Geophysical Research*, *102*(C13), 27,751–27,769. https://doi.org/10.1029/97JC02327

Gent, P. R. (1981). Forced standing equatorial ocean wave modes. *Journal of Marine Research*, *39*, 695–709.

Gent, P. R., O'Neill, K., & Cane, M. A. (1983). A model of the semiannual oscillation in the equatorial Indian Ocean. *Journal of Physical Oceanography*, *13*(12), 2148–2160. https://doi.org/10.1175/1520-0485(1983)013<2148:AMOTSO>2.0.CO;2

Gill, A. E. (1982). *Atmosphere–ocean dynamics*. Orlando: Academic.

Gouriou, Y., Delcroix, T., & Eldin, G. (2006). Upper and intermediate circulation in the western equatorial Pacific Ocean in October 1999 and April 2000. *Geophysical Research Letters*, *33*, L10603. https://doi.org/10.1029/2006GL025941

Han, W., McCreary, P. J., Anderson, D. L. T., & Mariano, A. J. (1999). Dynamics of the eastern surface jets in the equatorial Indian Ocean. *Journal of Physical Oceanography*, *29*(9), 2191–2209. https://doi.org/10.1175/1520-0485(1999)029<2191:Dotesj>2.0.Co;2

Han, W., McCreary, P. J., Masumoto, Y., Vialard, J., & Duncan, B. (2011). Basin resonances in the equatorial Indian Ocean. *Journal of Physical Oceanography*, *41*(6), 1252–1270. https://doi.org/10.1175/2011jpo4591.1

Horel, J. D. (1984). Complex principal component analysis—Theory and examples. *Journal of Climate and Applied Meteorology*, *23*(12), 1660–1673. https://doi.org/10.1175/1520-0450(1984)023<1660:Cpcata>2.0.Co;2

Huang, K., Han, W., Wang, D., Wang, W., Xie, Q., Chen, J., & Chen, G. (2018). Features of the Equatorial Intermediate Current associated with basin resonance in the Indian Ocean. *Journal of Physical Oceanography*, *48*, 1333–1347. https://doi.org/10.1175/JPO-D-17-0238.1

Iskandar, I., Masumoto, Y., & Mizuno, K. (2009). Subsurface equatorial zonal current in the eastern Indian Ocean. *Journal of Geophysical Research, Oceans*, *114*, C06005. https://doi.org/10.1029/2008JC005188

Jensen, T. G. (1993). Equatorial variability and resonance in a wind-driven Indian-Ocean model. *Journal of Geophysical Research*, *98*(C12), 22,533–22,552. https://doi.org/10.1029/93JC02565

Kawase, M. (1987). Establishment of deep ocean circulation driven by deep-water production. *Journal of Physical Oceanography*, *17*(12), 2294–2317. https://doi.org/10.1175/1520-0485(1987)017<2294:Eodocd>2.0.Co;2

Kessler, W. S., & McCreary, J. P. (1993). The annual wind-driven Rossby-wave in the subthermocline equatorial Pacific. *Journal of Physical Oceanography*, *23*(6), 1192–1207. https://doi.org/10.1175/1520-0485(1993)023<1192:Tawdrw>2.0.Co;2

Knox, R. A. (1974). Reconnaissance of the Indian Ocean equatorial undercurrent near Addu Atoll. *Deep Sea Research and Oceanographic Abstracts*, *21*(2), 123–129. https://doi.org/10.1016/0011-7471(74)90069-2

Locarnini, R. A., Mishonov, A. V., Antonov, J. I., Boyer, T. P., & Garcia, H. E. (2006). *World Ocean Atlas 2005, Vol. 1: Temperature, NOAA Atlas NESDIS* (Vol. 61, p. 182). Washington, DC: U.S. Government Printing Office.

Lukas, R., & Firing, E. (1985). The annual Rossby-wave in the central equatorial Pacific Ocean. *Journal of Physical Oceanography*, *15*(1), 55–67. https://doi.org/10.1175/1520-0485(1985)015<0055:Tarwit>2.0.Co;2

Luyten, J. R., & Roemmich, D. H. (1982). Equatorial currents at semiannual period in the Indian Ocean. *Journal of Physical Oceanography*, *12*(5), 406–413. https://doi.org/10.1175/1520-0485(1982)012<0406:Ecasap>2.0.Co;2

Luyten, J. R., & Swallow, J. C. (1976). Equatorial undercurrents. *Deep Sea Research*, *23*(10), 999–1001. https://doi.org/10.1016/0011-7471(76)90830-5

Madec, G. (2008). NEMO reference manual, ocean dynamics component: NEMO-OPA. Preliminary version, *Note du Pole de Model. 27,* Inst. Pierre–Simon Laplace, Paris, France.

Marin, F., Kestenare, E., Delcroix, T., Durand, F., Cravatte, S., Eldin, G., & Bourdalle-Badie, R. (2010). Annual reversal of the equatorial intermediate current in the Pacific: Observations and model diagnostics. *Journal of Physical Oceanography*, *40*(5), 915–933. https://doi.org/10.1175/2009jpo4318.1

Matsuno, T. (1966). Quasi-geostrophic motions in the equatorial area. *Journal of the Meteorological Society of Japan*, *44*(1), 25–43. https://doi.org/10.2151/jmsj1965.44.1_25

McCreary, J. P. (1984). Equatorial beams. *Journal of Marine Research*, *42*(2), 395–430. https://doi.org/10.1357/002224084788502792

McPhaden, M. J. (1982). Variability in the central equatorial Indian-Ocean. 1. Ocean dynamics. *Journal of Marine Research*, *40*(1), 157–176.

McPhaden, M. J., Meyers, G., Ando, K., Masumoto, Y., Murty, V. S. N., Ravichandran, M., et al. (2009). RAMA: The Research Moored Array for African-Asian-Australian Monsoon Analysis and Prediction. *Bulletin Of The American Meteorological Society*, *90*(4), 459–480. https://doi.org/10.1175/2008BAMS2608.1

Mogensen, K., Alonso Balmaseda, M., & Weaver, A. (2012). The NEMOVAR ocean data assimilation system as implemented in the ECMWF ocean analysis for System4. *ECMWF Thechnical Memorandum 668*.59 Pages.

Moore, D. W., & Philander, S. G. H. (1977). Modeling of the tropical ocean circulation. Marine Modeling. In E. D. Goldberg, et al. (Eds.), *The sea* (Vol. 6, pp. 319–361). New York: John Wiley Interscience.

Murty, V. S. N., Suryanarayana, A., Sarma, M. S. S., Tilvi, V., Fernando, V., Nampoothiri, G., et al. (2002). First results of Indian current meter moorings along the equator: Vertical current structure variability at equator, 93°E during February–December 200. Proc. 6th Pan Ocean Remote Sensing Conference, PORSEC 2002, Bali, Indonesia, 1, 25–28.

Murty, V. S. N., Sarma, M. S. S., Suryanarayana, A., Sengupta, D., Unnikrishnan, A. S., Fernando, V., et al. (2006). Indian moorings: Deep-sea current meter moorings in the eastern equatorial Indian Ocean. *CLIVAR Exchanges*, *11*(4), 5–8.

Nagura, M., & Masumoto, Y. (2015). A Wake due to the Maldives in the Eastward Wyrtki Jet. *Journal of Physical Oceanography*, *45*(7), 1858–1876. https://doi.org/10.1175/JPO-D-14-0191.1

Nagura, M., & McPhaden, M. J. (2010). Wyrtki Jet dynamics: Seasonal variability. *Journal of Geophysical Research*, *115*, C07009. https://doi.org/10.1029/2009JC005922

Nagura, M., & McPhaden, M. J. (2014). Zonal momentum budget along the equator in the Indian Ocean from a high-resolution ocean general circulation model. *Journal of Geophysical Research: Oceans*, *119*, 4444–4461. https://doi:10.1002/2014JC009895

Nagura, M., & McPhaden, M. J. (2016). Zonal propagation of near-surface zonal currents in relation to surface wind forcing in the equatorial Indian Ocean. *Journal of Physical Oceanography*, *46*(12), 3623–3638. https://doi.org/10.1175/Jpo-D-16-0157.1

Nyadjro, E. S., & McPhaden, M. J. (2014). Variability of zonal currents in the eastern equatorial Indian Ocean on seasonal to interannual time scales. *Journal of Geophysical Research: Oceans*, *119*, 7969–7986. https://doi.org/10.1002/2014JC010380

Ogata, T., & Xie, S. P. (2011). Semiannual cycle in zonal wind over the equatorial Indian Ocean. *Journal of Climate*, *24*(24), 6471–6485. https://doi.org/10.1175/2011jcli4243.1

Philander, S. G. H. (1978). Forced oceanic waves. *Reviews of Geophysics*, *16*(1), 15–46. https://doi.org/10.1029/RG016i001p00015

Philander, S. G. H., & Chao, Y. (1991). On the contrast between the seasonal cycle of the equatorial Atlantic and Pacific Oceans. *Journal of Physical Oceanography*, *21*(9), 1399–1406. https://doi.org/10.1175/1520-0485(1991)021<1399:OTCBTS>2.0.CO;2

Rao, R. R., Horii, T., Masumoto, Y., & Mizuno, K. (2017). Observed variability in the upper layers at the equator, 90°E in the Indian Ocean during 2001–2008, 2: Meridional currents. *Climate Dynamics*, *49*(3), 1031–1048. https://doi.org/10.1007/s00382-016-2979-9

Sengupta, D., Senan, R., Goswami, B. N., & Vialard, J. (2007). Intraseasonal variability of equatorial Indian Ocean zonal currents. *Journal of Climate*, *20*(13), 3036–3055. https://doi.org/10.1175/Jcli4166.1

Thierry, V., Treguier, A. M., & Mercier, H. (2004). Numerical study of the annual and semi-annual fluctuations in the deep equatorial Atlantic Ocean. *Ocean Modelling*, *6*(1), 1–30. https://doi.org/10.1016/S1463-5003(02)00054-9

Thomson, D. J. (1982). Spectrum estimation and harmonic-analysis. *Proceedings of the IEEE*, *70*(9), 1055–1096. https://doi.org/10.1109/Proc.1982.12433

Uppala, S. M., KÅllberg, P. W., Simmons, A. J., Andrae, U., Bechtold, V. D. C., Fiorino, M., et al. (2005). The ERA-40 re-analysis. *Quarterly Journal of the Royal Meteorological Society*, *131*(612), 2961–3012. https://doi.org/10.1256/qj.04.176

Wang, D., Liu, Q. Y., Liu, Y., & Shi, P. (2004). Connection between interannual variability of the western Pacific and eastern Indian Oceans in the 1997–1998 El Niño event. *Progress in Natural Science*, *14*(5), 423–429.

Wang, F., Wang, J. N., Guan, C., Ma, Q., & Zhang, D. X. (2016). Mooring observations of equatorial currents in the upper 1000 m of the western Pacific Ocean during 2014. *Journal of Geophysical Research: Oceans*, *121*, 3730–3740. https://doi.org/10.1002/2015JC011510

Weisberg, R. H., & Wang, C. (1997). Slow variability in the equatorial west-central Pacific in relation to ENSO. *Journal of Climate*, *10*(8), 1998–2017. https://doi.org/10.1175/1520-0442(1997)010<1998:SVITEW>2.0.CO;2

Wyrtki, K. (1973). An equatorial jet in the Indian Ocean. *Science*, *181*(4096), 262–264. https://doi.org/10.1126/science.181.4096.262

Yamagata, T., Mizuno, K., & Masumoto, Y. (1996). Seasonal variations in the equatorial Indian Ocean and their impact on the Lombok throughflow. *Journal of Geophysical Research*, *101*(C5), 12,465–12,473. https://doi.org/10.1029/95JC03623

Youngs, M. K., & Johnson, G. C. (2015). Basin-wavelength equatorial deep jet signals across three oceans. *Journal of Physical Oceanography*, *45*(8), 2134–2148. https://doi.org/10.1175/Jpo-D-14-0181.1

Yuan, D. L., & Han, W. Q. (2006). Roles of equatorial waves and western boundary reflection in the seasonal circulation of the equatorial Indian Ocean. *Journal of Physical Oceanography*, *36*(5), 930–944. https://doi.org/10.1175/Jpo2905.1